

Supporting Information for

## Creation of Single-Photon Emitters in WSe<sub>2</sub> Monolayers Using Nanometer-Sized Gold Tips

Lintao Peng,<sup>1</sup> Henry Chan,<sup>1</sup> Priscilla Choo,<sup>2,3</sup> Teri W. Odom,<sup>2,3</sup> Subramanian K. R. S.

Sankaranarayanan,<sup>1,4</sup> Xuedan Ma<sup>1</sup>

<sup>1</sup>Center for Nanoscale Materials, Argonne National Laboratory, Lemont, Illinois 60439, United States

<sup>2</sup>Department of Chemistry, Northwestern University, Evanston, Illinois 60208, United States

<sup>3</sup>Department of Materials Science and Engineering, Northwestern University, Evanston, Illinois 60208, United States

<sup>4</sup>Department of Mechanical and Industrial Engineering, University of Illinois, Chicago, IL 60607

### S1. Details of the experimental methods and molecular dynamics simulations

**Synthesis of gold nanostars.** Nanostars were synthesized via a seedless growth method, where (4-(2-hydroxyethyl)-1-piperazineethanesulfonic acid) (HEPES) buffer functions both as a nucleation and a shape-directing agent. 1 M stock HEPES solutions were purchased from Sigma-Aldrich and their pH was adjusted to 7.38 using concentrated NaOH solutions. Nanostars were synthesized by adding 0.2 mM (final concentration) gold (III) chloride trihydrate (HAuCl<sub>4</sub>) to 110 mM HEPES buffer and vortexing for one minute after HAuCl<sub>4</sub> addition to final volume of 20 mL. The growth solution was left in dark for 24 hours to allow for growth and stabilization.

**Preparation of the TMD samples.** WSe<sub>2</sub> monolayers used in this study were prepared by mechanical exfoliation of bulk materials. As-synthesized AuNS stock solutions were washed with deionized water and their droplets with optimal concentrations were then deposited onto the WSe<sub>2</sub> monolayers to form the hybrid structures for characterizations. To count the number of quantum emitters per site, the concentrations of the AuNS on the WSe<sub>2</sub> monolayers were kept sufficiently low with an average separation distance of larger than 1 μm<sup>2</sup>. For the reference samples, dielectric

nanopillars with a height of around 85 nm and a diameter of around 200 nm were fabricated by electron-beam lithography. Specifically, thin layers of photoresist (hydrogen silsesquioxane) with a thickness of around 85 nm were spin-coated onto silicon substrates. Arrays of nanopillars with a diameter of 200 nm and spacing of 3  $\mu\text{m}$  were exposed by electron beam and then developed with microposit MF-CD 26 and cleaned with DI water. The heights and diameters of the nanopillars were measured using scanning electron microscopy and atomic force microscopy. WSe<sub>2</sub> monolayers were then transferred onto the nanopillars using the polycarbonate-based dry stamping method.<sup>1</sup>

**Low-temperature single-particle measurements.** The prepared TMD samples were loaded into a continuous-flow liquid He cryostat on a home-built confocal laser microscope. A diode laser with a wavelength of 400 nm and adjustable lasing modes was used to excite the samples. It was tuned to the continuous-wave mode for static spectroscopic and imaging measurements, and to the pulsed mode (repetition frequency = 5 MHz) for the time-resolved measurements. The laser beam was focused by a microscope objective (40x, NA = 0.7) onto the samples. Photoluminescence from the samples was collected by the same objective and sent to a 500 mm spectrograph equipped with a charge-coupled device for imaging and spectroscopic measurements, or to single-photon avalanche diodes for time-resolved measurements. For the photon-correlation measurements, the photoluminescence signal was split by a 1:1 beamsplitter and sent to two identical single-photon avalanche diodes in the Hanbury-Brown and Twiss layout for coincidence event measurements.

**Molecular dynamics simulation of local strain field.** The interactions between W-W, Se-Se, W-Se, and Si-Si were modeled using the Tersoff potential with parameters obtained from Ref. 2 and Ref. 3. The interactions between Au-Au were modeled using the embedded-atom method (EAM) with parameters obtained from Ref. 4. The cross interactions between Si-Se, Si-W, Au-Se, and Au-W were modelled using the standard 12/6 Lennard Jones potential (13  $\text{\AA}$  cutoff) with parameters chosen to produce a WSe<sub>2</sub> monolayer that lays relatively flat on the substrate at the simulated temperature. The parameters for the cross interactions between W-W, Se-Se, W-Se, and Si-Si are listed here:  $\epsilon_{\text{Si-Se}} = 0.02088 \text{ eV}$ ,  $\sigma_{\text{Si-Se}} = 3.25 \text{ \AA}$ ,  $\epsilon_{\text{Si-W}} = 0.00364 \text{ eV}$ ,  $\sigma_{\text{Si-W}} = 3.46 \text{ \AA}$ ,  $\epsilon_{\text{Au-Se}} = 0.01088 \text{ eV}$ ,  $\sigma_{\text{Au-Se}} = 2.58 \text{ \AA}$ ,  $\epsilon_{\text{Au-W}} = 0.00364 \text{ eV}$ ,  $\sigma_{\text{Au-W}} = 2.80 \text{ \AA}$ . These cross-interaction parameters were chosen to produce a WSe<sub>2</sub> monolayer that lays relatively flat on the substrate while considering information from Ref. 5 and Ref. 6. As in the experiments, the deformation field

created by the AuNS was under the influence of (almost negligible) gravitational force but was included in the simulation.

In the simulations, the system was equilibrated for around 2 ns with the gold tip directly on top of the WSe<sub>2</sub> monolayer, followed by around 5 ps equilibration with the gold tip lifted to obtain a reference frame for subsequent atomic strain calculations. During the equilibration, we observed local reorganization of atoms in the gold tips (especially in tips that were in contact with the WSe<sub>2</sub> monolayer) and slight sliding of the WSe<sub>2</sub> monolayer on the silicon substrate. We calculated the local atomic strains of atoms within a 3 nm cutoff, which yielded smooth deformation values at the atomic sites without losing too much local details of the deformation field.

## **S2. Quantitative analysis of the strain maps obtained from molecular dynamics simulations**

The atomic strains obtained from the molecular dynamics simulations represent volumetric strains, *i.e.* local changes in volume before and after applying the strains (adding the AuNS in this case):  $\varepsilon_V = \Delta V/V_0$ . Here,  $\Delta V$  is the volume change caused by the strain and  $V_0$  is the volume before loading the strain. Depending on the nature of the loaded strain, this might be different from uniaxial strains, *i.e.* strains in the uniaxial loading direction only:  $\varepsilon_L = \Delta L/L_0$  with  $\Delta L$  being the length change in the loading direction and  $L_0$  the original length.

We perform quantitative analysis of the strain profiles caused by the AuNS. Fig. S1 below shows the population distributions of WSe<sub>2</sub> atoms with absolute strain values larger than 0%, 0.1%, 0.5%, 1%, and 1.3%, and the corresponding spatial locations of the atoms with these strain values. It can be observed that both compressive and tensile strains exist, with the former being stronger than the latter (notice the range of the negative strain values extend much further than the positive values). Although a maximum strain amplitude of 6% is observed, only around 2.4% of the atoms experience strain fields larger than 1.0%.

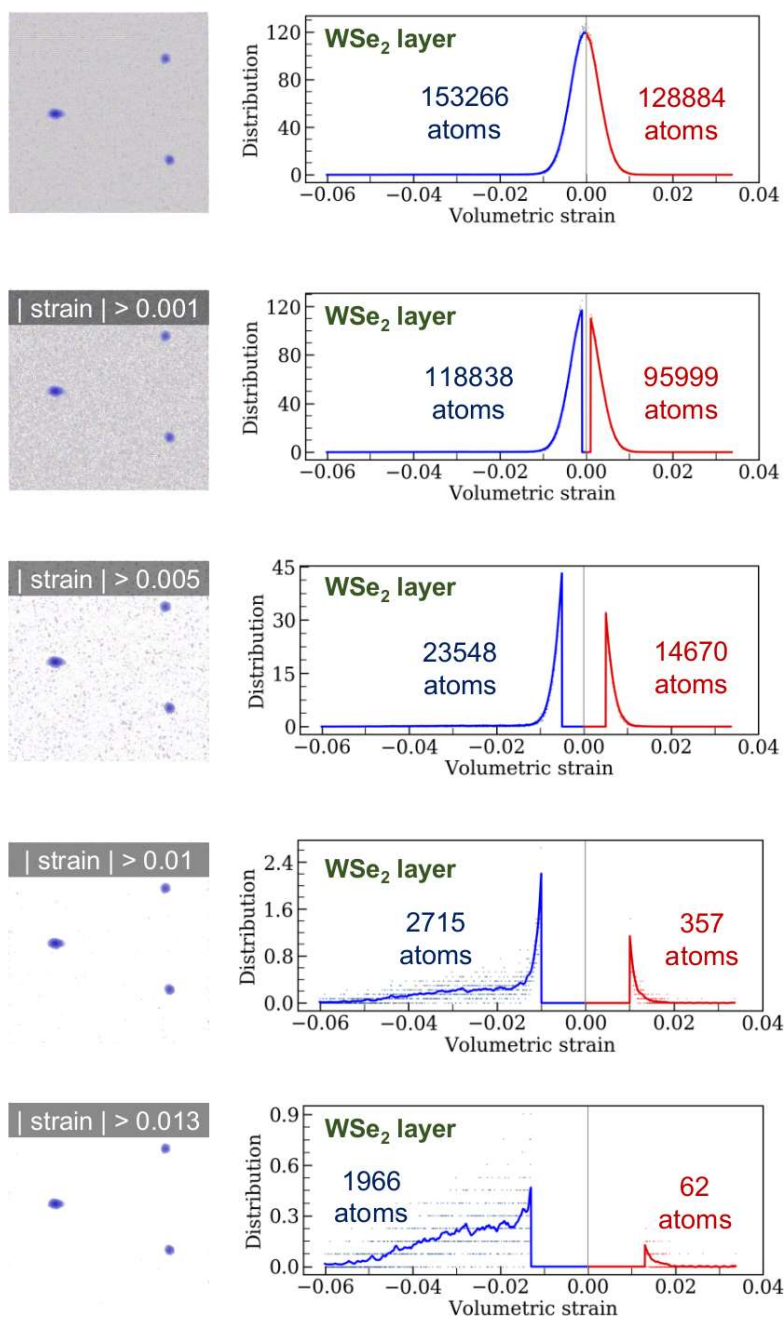


Figure S1. Left: Spatial distributions of WSe<sub>2</sub> atoms with absolute strain values larger than 0%, 0.1%, 0.5%, 1.0%, and 1.3%. Right: Population distributions of WSe<sub>2</sub> atoms with absolute strain values larger than 0%, 0.1%, 0.5%, 1%, and 1.3%.

### S3. AuNS-induced quantum emitters in WSe<sub>2</sub> monolayers

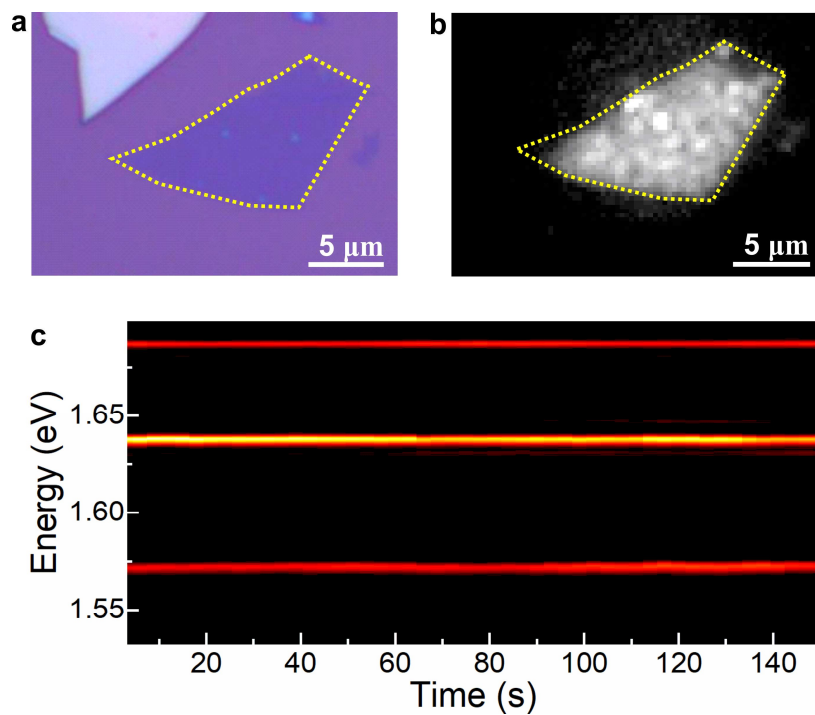


Figure S2. (a) Optical micrograph of a monolayer WSe<sub>2</sub> flake. (b) Photoluminescence image of the monolayer WSe<sub>2</sub> flake in (a) after being deposited with AuNS. Dense distributions of bright, localized emission spots can be observed. (c) Example of photoluminescence spectra taken from a bright spot in (b).

#### S4. Examples of quantum emitters created by dielectric nanopillars

Fig. S3 below shows representative data of quantum emitters created by dielectric nanopillars.

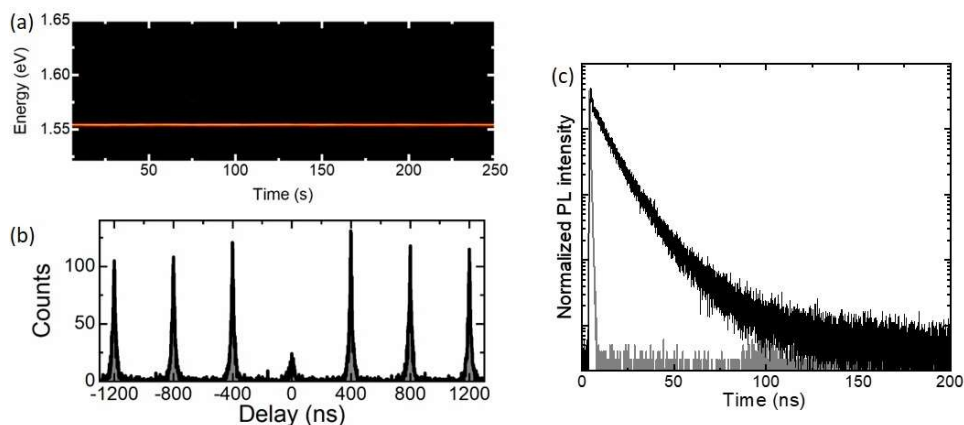


Figure S3. Representative time-dependent PL spectra (a), second-order photon correlation curve (b), and PL decay curve (c) from a quantum emitter created by dielectric nanopillars.

### S5. PL intensity-dependent lifetime analysis of the quantum emitters

Fig. S4a below shows a representative PL time trace of a quantum emitter in a WSe<sub>2</sub> monolayer. PL blinking can be observed, giving rise to two predominant PL intensity peaks (Fig. S4b). To investigate the PL intensity dependent lifetimes, we extract PL decays from the “on” (Fig. S4a, blue) and “off” (Fig. S4a, orange) periods (Fig. S4c, d). Fitting of the two decay curves leads to average lifetimes of 6.3 ns for the off period, and 8.1 ns for the on period.

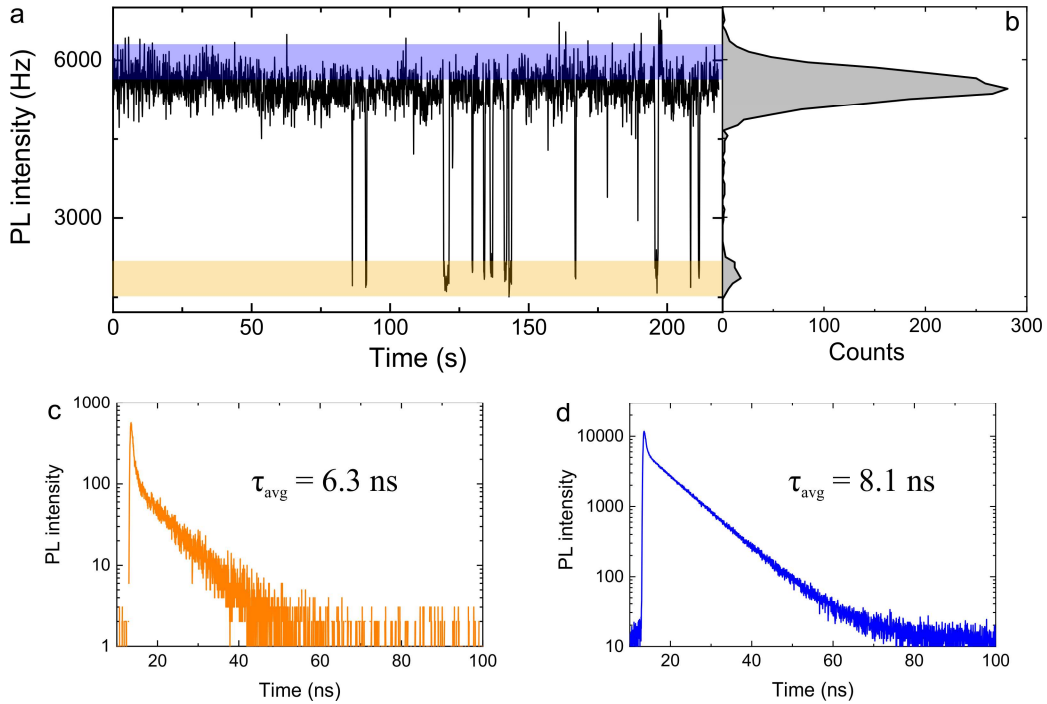


Figure S4. (a) A representative PL time trace of a quantum emitter in a WSe<sub>2</sub> monolayer. (b) The corresponding count rate histograms of the PL time trace in (a). (c, d) PL decay curves constructed from the photons in the on (blue) and off (orange) periods in (a).

### S6. Numerical simulations of the PL decay rate and quantum efficiency

We perform 3D finite-difference time-domain simulations to obtain information about the local electric field enhancement and changes in the radiative and nonradiative decay rates of the quantum emitters.<sup>7</sup> Since the PL intensity  $I = \sigma \cdot \text{QE}$ , where  $\sigma$  is the absorption cross section of the quantum emitters at the excitation wavelength and  $\text{QE} = \frac{k_r}{k_r + k_{nr}}$ , using the experimentally observed  $I/I_0 = 1.4$  ( $I_0$  being the average PL intensity of the uncoupled quantum emitters and  $I$  the average PL intensity of the surface plasmon-affected quantum emitters), simulation obtained  $\sigma/\sigma_0 \sim 5$  (at the excitation wavelength of 400 nm) and  $k_r/k_{r,0}$  and  $k_{nr}/k_{r,0}$  values, we can derive the quantum efficiencies of the emitters created by the AuNS (QE) and dielectric nanopillars (QE<sub>0</sub>) (see Table S1 below). It can be seen that the locations of the created quantum emitters and the orientations of their transition dipoles have strong influences on the decay rates and quantum efficiencies. If we average over all the locations and dipole orientations in Table 1 with the simple assumption that the three arms of the AuNS have similar probabilities of generating quantum emitters, we obtain an average uncoupled quantum efficiency QE<sub>0</sub> of 3.3%, which is in an excellent agreement with previously reported values.<sup>8</sup> This simple assumption also gives an average Purcell factor of 30.

Table S1. Numerical simulation obtained exciton dynamics and quantum efficiencies

Location	Orientation	Distance (nm)	$k_r/k_{r,0}$	$k_{nr}/k_{r,0}$	QE <sub>0</sub> (%)	QE (%)
Long arm <sup>1</sup>	Length <sup>2</sup>	1	197	56700	1.3	0.34
Long arm	Length	2	31	6300	1.8	0.49
Long arm	Width	1	0.79	78	2.4	0.66
Long arm	Width	2	0.91	6300	0.035	0.001
Short arm	Length	1	0.67	258	0.54	0.15
Short arm	Length	2	0.96	41.7	6.0	1.6
Short arm	Width	1	3.4	360	3.1	0.86
Short arm	Width	2	5.1	148	11.4	3.2
Average			30.0	8773	3.3	0.91

<sup>1</sup>Long/Short arm refers to the emitter lying underneath the long/short arm of the AuNS.

<sup>2</sup>Length/Width refers to the transition dipole of the emitter lying along the long/short arm of the AuNS.

## S7. Histograms of PL intensities of quantum emitters created by AuNS and dielectric nanopillars

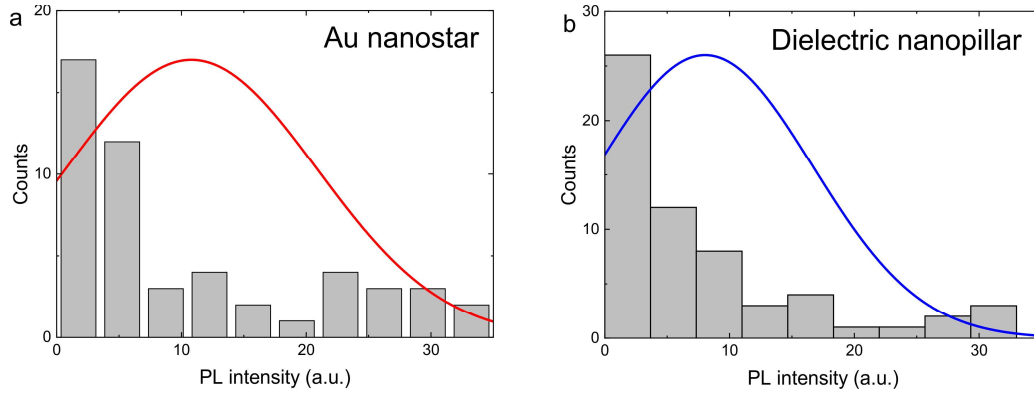


Figure S5. Histograms of PL intensities of quantum emitters created by AuNS and dielectric nanopillars.

### S8. Second-order photon correlation spectroscopy of quantum emitters

Fig. S6 below shows the second-order photon correlation spectrum of a quantum emitter in monolayer WSe<sub>2</sub> for timescales up to 15  $\mu$ s. Slight photon-bunching in the side peak accompanying the photon antibunching dip at delay time  $\tau = 0$  can be observed. This kind of correlation profile has been observed in other types of quantum emitters and attributed to the existence of a dark state that traps excitons and prevents the subsequent emission of a photon in a certain time.<sup>9-11</sup> We infer that a similar dark state exists in the quantum emitters in monolayer

WSe<sub>2</sub>. Using the model developed by Santori *et al.*:<sup>12</sup>  $g^{(2)}(\tau) = 1 + \frac{\tau_{\text{off}}}{\tau_{\text{on}}} e^{-\left(\frac{1}{\tau_{\text{on}}} + \frac{1}{\tau_{\text{off}}}\right)|\tau|}$  to fit the  $g^{(2)}(\tau)$  curve, we obtain lifetimes for the bright and dark states of  $\tau_{\text{on}} = 9.5$  ns and  $\tau_{\text{off}} = 61.3$   $\mu$ s, respectively.

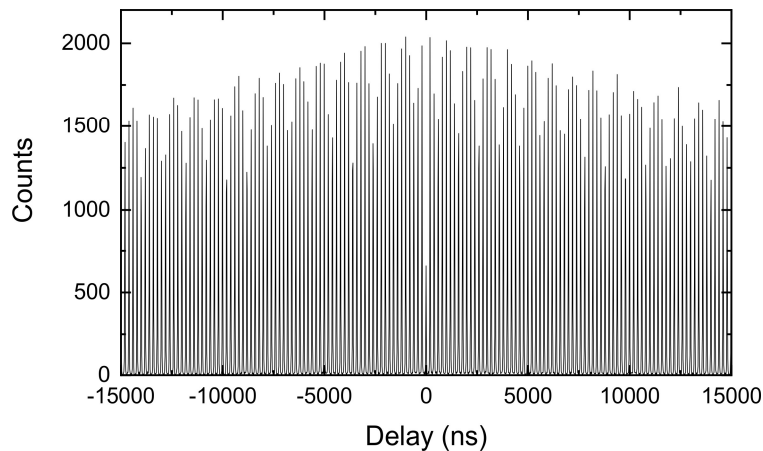


Figure S6. Second-order photon correlation spectrum of a quantum emitter in monolayer WSe<sub>2</sub>. Photon-bunching in the side peak can be observed.

### S9. Calculations of the strain-induced bright-dark splitting

The distribution of the exciton populations in the bright ( $n_B$ ) and dark ( $n_D$ ) states can be represented by the Boltzmann distribution:  $n_B = e^{-\varepsilon_B/k_B T}$  and  $n_D = e^{-\varepsilon_D/k_B T}$ , where  $\varepsilon_B$  and  $\varepsilon_D$  are the energies of the bright and dark states, respectively. The PL intensity ratio between the bright and dark states can be represented as  $\frac{I_B}{I_D} \propto \frac{n_B}{n_D} = e^{-\Delta E/k_B T}$  with  $\Delta E = \varepsilon_B - \varepsilon_D$ . Assume that the tensile and compressive strains change the dark-bright energy splitting by  $\Delta E_T$  and  $\Delta E_C$ , respectively. The corresponding energy splitting for the quantum emitters experiencing tensile and compressive strains becomes  $\Delta E - \Delta E_T$  and  $\Delta E + \Delta E_C$ , respectively. The PL intensity ratio of a quantum emitter subject to tensile and compressive strains can then be represented by  $\eta = e^{(\Delta E_T + \Delta E_C)/k_B T}$ . The average PL intensity ratios  $\bar{\eta}$  between the two groups of emitters for Fig. 4c and 4d are estimated to be around 1.30 and 1.36, respectively. This gives rise to  $\Delta E_T + \Delta E_C$  of around 0.55 meV and 0.57 meV for the AuNS- and nanopillar-induced quantum emitters, respectively. According to previous theoretical calculations by Johari *et al.*,<sup>13</sup> the corresponding strain amplitudes that would give rise to this level of changes in the dark-bright energy splitting should be on the order of 0 – 2 %, agreeing well with our molecular dynamics simulations and previously reported strain values for WSe<sub>2</sub> monolayers on dielectric nanopillars.<sup>8, 14</sup>

#### Reference:

1. Zomer, P. J., Guimarães, M. H. D., Brant, J. C., Tombros, N., van Wees, B. J. Fast pick up technique for high quality heterostructures of bilayer graphene and hexagonal boron nitride. *Appl. Phys. Lett.* **2014**, *105*, 013101.
2. Chan, H., Sasikumar, K., Srinivasan, S., Cherukara, M., Narayanan, B., Sankaranarayanan, S. K. R. S. Machine learning a bond order potential model to study thermal transport in WSe<sub>2</sub> nanostructures. *Nanoscale* **2019**, *11*, 10381-10392.

3. Tersoff, J. Modeling solid-state chemistry: Interatomic potentials for multicomponent systems. *Phys. Rev. B* **1989**, *39*, 5566(R).
4. Foiles, S. M., Baskes, M. I., Daw, M. S. Embedded-atom-method functions for the fcc metals Cu, Ag, Au, Ni, Pd, Pt, and their alloys. *Phys. Rev. B* **1986**, *44*, 7983.
5. Wang, Y., Kim, J. C., Wu, R. J., Martinez, J., Song, X., Yang, J., Zhao, F., Mkhoyan, A., Jeong, H. Y., Chhowalla, M. Van der Waals contacts between three-dimensional metals and two-dimensional semiconductors. *Nature* **2019**, *568*, 70-74.
6. Ryu, S., Cai, W. A gold–silicon potential fitted to the binary phase diagram. *J. Phys.: Condens. Mater.* **2010**, *22*, 055401.
7. Ma, X.; Fletcher, K.; Kipp, T.; Grzelczak, M. P.; Wang, Z.; Guerrero-Martínez, A.; Pastoriza-Santos, I.; Kornowski, A.; Liz-Marzán, L. M.; Mews, A. Photoluminescence of Individual Au/CdSe Nanocrystal Complexes with Variable Interparticle Distances. *J. Phys. Chem. Lett.* **2011**, *2*, 2466-2471.
8. Luo, Y.; Shepard, G. D.; Ardelean, J. V.; Rhodes, D. A.; Kim, B.; Barmak, K.; Hone, J. C.; Strauf, S. Deterministic coupling of site-controlled quantum emitters in monolayer WSe<sub>2</sub> to plasmonic nanocavities. *Nat. Nanotechnol.* **2018**, *13*, 1137-1142.
9. Ma, X.; Hartmann, N. F.; Baldwin, J. K. S.; Doorn, S. K.; Htoon, H. Room-temperature single-photon generation from solitary dopants of carbon nanotubes. *Nat. Nanotechnol.* **2015**, *10*, 671-675.
10. Berthel, M.; Mollet, O.; Dantelle, G.; Gacoin, T.; Huant, S.; Drezet, A. Photophysics of single nitrogen-vacancy centers in diamond nanocrystals. *Phys. Rev. B* **2015**, *91*, 035308.
11. Gali, A.; Maze, J. R. Ab initio study of the split silicon-vacancy defect in diamond: Electronic structure and related properties. *Phys. Rev. B* **2013**, *88*, 235205.
12. Santori, C.; Pelton, M.; Solomon, G.; Dale, Y.; Yamamoto, Y. Triggered single photons from a quantum dot. *Phys. Rev. Lett.* **2001**, *86*, 1502-1505.
13. Johari, P.; Shenoy, V. B. Tuning the Electronic properties of semiconducting transition metal dichalcogenides by applying mechanical strains. *ACS Nano* **2012**, *6*, 5449-5456.
14. Branny, A.; Kumar, S.; Proux, R.; Gerardot, B. D. Deterministic strain-induced arrays of quantum emitters in a two-dimensional semiconductor. *Nat. Commun.* **2017**, *8*, 15053.